

Multifunctional Cu_2TSiS_4 (T = Mn and Fe): Polar Semiconducting Antiferromagnets with Nonlinear Optical Properties

Zachary T. Messegee, Jun Sang Cho, Andrew J. Craig, V. Ovidiu Garlea, Yan Xin, Chang-Jong Kang, Thomas E. Proffen, Hari Bhandari, Jordan C. Kelly, Nirmal J. Ghimire, Jennifer A. Aitken, Joon I. Jang,* and Xiaoyan Tan*



Cite This: *Inorg. Chem.* 2023, 62, 530–542



Read Online

ACCESS |



Metrics & More

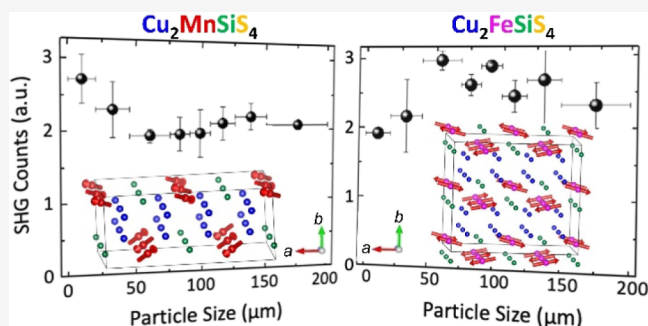


Article Recommendations



Supporting Information

ABSTRACT: Cu_2TSiS_4 (T = Mn and Fe) polycrystalline and single-crystal materials were prepared with high-temperature solid-state and chemical vapor transport methods, respectively. The polar crystal structure (space group $Pmn2_1$) consists of chains of corner-sharing and distorted CuS_4 , Mn/Fe S_4 , and SiS_4 tetrahedra, which is confirmed by Rietveld refinement using neutron powder diffraction data, X-ray single-crystal refinement, electron diffraction, energy-dispersive X-ray spectroscopy, and second harmonic generation (SHG) techniques. Magnetic measurements indicate that both compounds order antiferromagnetically at 8 and 14 K, respectively, which is supported by the temperature-dependent (100–2 K) neutron powder diffraction data. Additional magnetic reflections observed at 2 K can be modeled by magnetic propagation vectors $k = (1/2, 0, 1/2)$ and $k = (1/2, 1/2, 1/2)$ for $\text{Cu}_2\text{MnSiS}_4$ and $\text{Cu}_2\text{FeSiS}_4$, respectively. The refined antiferromagnetic structure reveals that the Mn/Fe spins are canted away from the ac plane by about 14° , with the total magnetic moments of Mn and Fe being $4.1(1)$ and $2.9(1) \mu_B$, respectively. Both compounds exhibit an SHG response with relatively modest second-order nonlinear susceptibilities. Density functional theory calculations are used to describe the electronic band structures.



INTRODUCTION

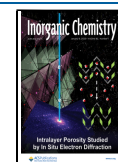
Cu_2TMS_4 (T = Mn, Fe, Co, Ni, Cu, Zn, Cd, and Hg; M = Si, Ge, and Sn), simplified as CTMS, and related quaternary chalcogenides are important semiconductors that have various optoelectronic and energy-related applications such as nonlinear optics,¹ solar cell technology,^{2,3} gamma-ray detectors,⁴ supercapacitors,⁵ and thermoelectric materials.^{6–8} CTMS compounds adopt either the tetragonal stannite ($I4_2m$),⁹ tetragonal kesterite ($I4$),¹⁰ tetragonal pseudo-cubic ($P4$),¹¹ or orthorhombic wurtz-stannite ($Pmn2_1$) structure types.¹² While the three tetragonal structure types are nonpolar, wurtz-stannite (WSt) possesses a polar crystal structure. The most common crystal structure type for CTMS compounds is stannite (St), for example, $\text{Cu}_2\text{FeSnS}_4$, which is a superstructure derived from sphalerite (Sp) such as $a_{\text{St}} \sim a_{\text{Sp}}, c_{\text{St}} \sim 2 a_{\text{Sp}}$.¹² The polar WSt crystal structure is a superstructure of wurtzite (W) via doubling of the unit cell along the a axis ($a_{\text{WSt}} \sim 2 a_w; b_{\text{WSt}} \sim \sqrt{3} a_w; c_{\text{WSt}} \sim c_w$), with the same metal-sulfur coordination environment as in St.¹² The only CTMS compounds reported thus far with the polar WSt crystal structure are $\text{Cu}_2\text{MnGeS}_4$ and Cu_2TSiS_4 (T = Mn and Fe).¹²

Most reported CTMS compounds are semiconducting antiferromagnets with antiferromagnetic (AFM) ordering transitions at low temperatures. $\text{Cu}_2\text{MnGeS}_4$ shows AFM

ordering near 8 K and adopts a magnetic space group P_2c with a magnetic propagation vector $k = (1/2, 0, 1/2)$, and spins are antiferromagnetically coupled in a collinear arrangement.¹³ The same magnetic propagation vector $k = (1/2, 0, 1/2)$ is also observed in $\text{Cu}_2\text{MnSnS}_4$ and $\text{Cu}_2\text{FeGeS}_4$ (space group $I4_2m$),^{14,15} but the collinear AFM magnetic structure (the magnetic space group is P_2c) in $\text{Cu}_2\text{MnSnS}_4$ is different from that in $\text{Cu}_2\text{MnGeS}_4$,¹⁴ and the final magnetic model of $\text{Cu}_2\text{FeGeS}_4$ is not determined.¹⁵ Cu_2TSiS_4 (T = Mn and Fe) are reported as antiferromagnets with a Néel temperature (T_N) of 8 and 15 K, respectively, and predicted to be multiferroic materials,^{16,17} but the magnetic structures remain unexplored. For multiferroic materials, an understanding of magnetic structures is important. Since different magnetic structures have been observed in the CTMS family, it would be interesting to reveal the magnetic structures in Cu_2TSiS_4 (T = Mn and Fe).

Received: October 24, 2022

Published: December 20, 2022



CTMS belongs to the large family of $AB^{\text{II}}M^{\text{IV}}X_4$ (A = alkali metals, Cu, and Ag; B = alkaline earth metals, transitional metals, Pb, and Eu; M = Si, Ge, and Sn; X = O, S, Se, and Te) compounds, which are also good candidates for nonlinear optical (NLO) materials. For example, $\text{Cu}_2\text{MnGeS}_4$ exhibits a strong SHG response with second-order NLO susceptibility, $\chi_S^{(2)} \sim 16.9$ pm/V, at room temperature.¹ Similarly, $\text{Li}_2\text{CdGeS}_4$, with the same WSt crystal structure, shows a robust SHG response with $\chi_S^{(2)} \sim 22.5$ pm/V.^{18,19} Cu_2TSiS_4 (T = Mn and Fe) were determined to adopt polar crystal structures based on X-ray single crystal (for T = Mn) or powder (for T = Fe) diffraction data.^{12,20} However, the definitive confirmation of the polar crystal structures and NLO properties has not yet been investigated.

In this study, we use X-ray powder diffraction (XRPD), neutron powder diffraction (NPD), and transmission electron microscopy (TEM) techniques to confirm the reported polar crystal structure of Cu_2TSiS_4 (T = Mn and Fe). Here, we also report the magnetic properties, magnetic structures, optical transparency in the infrared region, and second-order NLO properties of Cu_2TSiS_4 (T = Mn and Fe) by magnetic measurements, temperature-dependent NPD, attenuated total reflectance (ATR), Fourier transform infrared (FT-IR) spectroscopy, and second-order NLO property measurements, respectively. We perform density functional theory calculations to reveal the detailed electronic band structures.

EXPERIMENTAL SECTION

Starting Materials and Synthesis. Cu_2TSiS_4 (T = Mn and Fe) samples were prepared by heating the mixture of Cu (99.999% mass fraction, Alfa Aesar), Si (99.999% mass fraction, Alfa Aesar), and S (99.5% mass fraction, Alfa Aesar) powders with either Mn (99.95% mass fraction, Alfa Aesar) or Fe (99.99% mass fraction, Alfa Aesar) powders that were thoroughly ground and pressed into a pellet (6 mm in diameter). All sample preparations were carried out inside an argon-filled glove box with an O_2 and H_2O concentration of less than 1 ppm. Each pellet was then loaded into a quartz tube that was sealed under a dynamic vacuum ($<10^{-3}$ Torr). The obtained ampoule was heated in a box furnace at 600 °C for 1 d and 900 °C for 3 d with heating and cooling rates of 100 and 150 °C/h, respectively, which is a modified heating profile based on the previous report.¹² Cu_2TSiS_4 (T = Mn and Fe) single crystals ($<1 \times 1.5 \times 0.3$ mm³) were grown via the chemical vapor transport (CVT) method with iodide as the transport agent. For the CVT method, the mixture of elements was heated with a similar heating profile as the solid-state method but with a longer dwelling time (5 d) at 900 °C.

X-ray and Neutron Powder Diffraction. Room-temperature laboratory XRPD patterns for the polycrystalline samples were collected with a scattering angle 2θ ranging from 10 to 70° for 30 min using a Rigaku Miniflex-600 benchtop X-ray powder diffractometer (Cu K_α , $\lambda = 1.5418$ Å). NPD data were collected for ~3 g of the microcrystalline Cu_2TSiS_4 (T = Mn and Fe) samples using a powder diffractometer POWGEN at the Spallation Neutron Source, Oak Ridge National Laboratory.²¹ A neutron band with a center wavelength of 2.67 Å was used to collect the data. NPD data were obtained at various temperatures between 100 and 2 K. Rietveld refinements and data analysis using the NPD data were carried out by employing the suite of FullProf programs.²² Magnetic structure symmetry analysis was performed with the computational tools at the Bilbao crystallographic server.²³

X-ray Single-Crystal Diffraction. X-ray single-crystal diffraction data for Cu_2TSiS_4 (T = Mn and Fe) were obtained at room temperature on a Rigaku XtaLAB Synergy-i diffractometer with a HyPix-Bantam direct photon-counting detector and Mo K_α radiation. Small single crystals were mounted on a loop and measured on the goniometer head of the diffractometer. Data reduction and absorption correction were carried out using the Rigaku CrysAlis^{Pro} package. The

crystal structure of Cu_2TSiS_4 (T = Mn and Fe) was solved with the space group $Pmn2_1$ and refined using the SHELX-2018 software.²⁴ A summary of data collection and refined structure parameters is presented in Table S1. The corresponding atomic positions and anisotropic thermal parameters are provided in Tables S2 and S3.

Transmission Electron Microscopy. TEM experiments were conducted with a probe-aberration-corrected sub-Å resolution JEOL JEM-ARM200cF microscope using an accelerating voltage of 200 kV. Polycrystalline Cu_2TSiS_4 (T = Mn and Fe) powders were crushed into thin, electron-transparent pieces, which were transferred onto a carbon-coated 200-mesh Cu TEM grid. For the $\text{Cu}_2\text{FeSiS}_4$ sample, a few single crystals were also used to prepare thin pieces in a similar way to that used for the Cu_2TSiS_4 (T = Mn and Fe) powder samples. Selected area electron diffraction (SAED) patterns were obtained along the [100] or [001] direction on a single-crystal piece, and the corresponding atomic resolution high-angle-annular-dark-field scanning transmission electron microscopy (HAADF-STEM) images were collected.

Chemical Analysis. Elemental analysis of Cu_2TSiS_4 (T = Mn and Fe) was performed on single crystals with an Octane Elect Plus energy-dispersive X-ray (EDX) spectroscopy system, an accessory of a JEOL JSM-IT500HRLV scanning electron microscope (SEM). The SEM images and elemental maps were collected with an accelerating voltage of 15 kV.

Magnetic Measurements. Cu_2TSiS_4 (T = Mn and Fe) powders were loaded in a plastic capsule inside a plastic straw for the magnetic property measurements with the quantum design DynaCool physical property measurement system. Zero-field-cooled (ZFC) and field-cooled (FC) protocols were used to measure the magnetic susceptibility between 1.8 and 300 K with an applied magnetic field (H) of 0.1 T. Isothermal field-dependent magnetization was measured at 1.8 and 300 K using H ranging ± 9 T.

Attenuated Total Reflectance–Fourier Transform Infrared Spectroscopy. Optical transparency data were collected with 256 scans from 400 to 4000 cm^{-1} using a Thermo Nicolet 380 FT-IR spectrometer with an ATR accessory. The OMNIC software was used to collect and analyze the spectra. This method, where a diamond crystal is in optical contact with the samples, results in the thickness-dependent effect on the intensity of the spectra being negligible.²⁵ This is due to the penetration depth into the sample approaching the lower limit of the particle size, approximately 2 μm , within the sample.

Second-Order NLO Property Measurements. Crystalline Cu_2TSiS_4 (T = Mn and Fe) powders were sieved into discrete particle size ranges of <20, 20–45, 45–75, 75–90, 90–106, 106–125, 125–150, and >150 μm by employing a collection of stainless-steel W.S. Tyler test sieves and a Gilson sieve shaker in order to investigate the phase-matching (PM) nature of the SHG of the samples. Each sample was enclosed in a glass capillary tube by flame sealing under the vacuum to prevent moisture and air exposure to the samples during measurements. The capillary tubes were mounted on a homemade sample holder, and the measured SHG efficiencies of the samples were compared to those of the optical-quality reference materials, AgGaS_2 (AGS) and AgGaSe_2 (AGSe), for the estimation of the second-order nonlinear susceptibility, $\chi^{(2)}$. Note that the particle size ranges for the AGS and AGSe benchmark materials obtained from G&H Cleveland are a bit dissimilar to those of the samples, but this does not influence our NLO property analysis.

SHG measurements were recorded at room temperature using an input wavelength of $\lambda = 1800$ nm. Coherent light with $\lambda = 1064$ nm was first generated by an EKSPLA PL-2250 series diode-pumped Nd:YAG laser with a pulse width of 30 ps and a repetition rate of 50 Hz to generate tunable pulses. The Nd:YAG laser pumped an EKSPLA Harmonics Unit H400, where the input beam frequency was tripled to 355 nm via a series of NLO beam mixing. Two beams of 355 and 1064 nm next passed into an EKSPLA PG403-SH-DFG Optical Parametric Oscillator consisting of four components: (i) a double-pass parametric generator, (ii) a single-pass parametric amplifier, (iii) a second harmonic generator, and (iv) a difference frequency generator. A full explanation of the laser and detection setup has been provided previously.²⁶

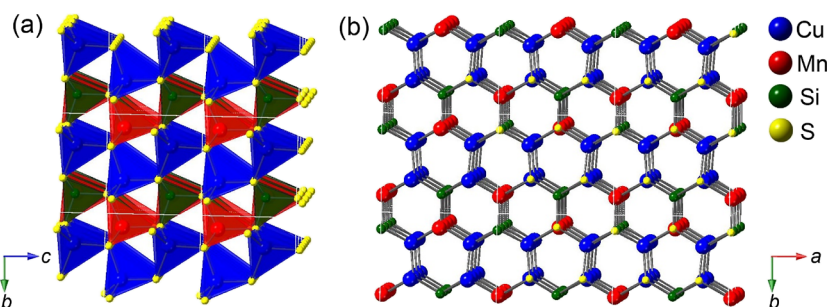


Figure 1. Perspective view of the crystal structure of $\text{Cu}_2\text{MnSiS}_4$ along the crystallographic a axis (a) and c axis (b).

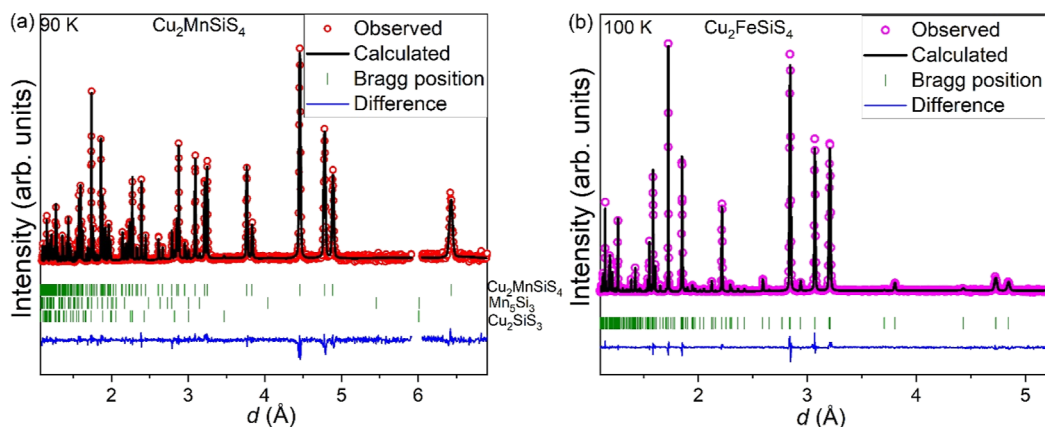


Figure 2. Rietveld refinement of $\text{Cu}_2\text{MnSiS}_4$ (a) and $\text{Cu}_2\text{FeSiS}_4$ (b) in the space group $Pmn2_1$ using NPD data. The observed data (red), the calculated pattern (black), and the difference between those two patterns (blue) are provided. The expected Bragg peak positions (green) of nuclear reflections are also depicted.

Density Functional Theory Calculations. The all-electron, full-potential linearized augmented plane-wave method implemented in WIEN2k was used to calculate the electronic structure.²⁷ Structural parameters were taken from NPD refinement. The Perdew–Burke–Ernzerhof generalized gradient approximation (GGA) was adopted for the exchange–correlation functional.²⁸ $14 \times 14 \times 22$ and $16 \times 17 \times 16$ k meshes were used in the Brillouin zone integration for $\text{Cu}_2\text{MnSiS}_4$ and $\text{Cu}_2\text{FeSiS}_4$, respectively. The muffin tin radii were chosen to be 2.37, 2.47, 2.36, 1.83, and 1.93 Bohr radii for Fe, Mn, Cu, Si, and S, respectively, and the size of a plane-wave basis set was determined from $R_{\text{mt}}K_{\text{max}}$ of 7.0, where R_{mt} is the smallest atomic muffin tin radius, and K_{max} is the largest plane-wave vector. To consider the strong correlation effect, GGA + U was adopted within the fully localized limit.^{29,30} The effective on-site Coulomb interaction parameters, $U_{\text{eff}} = U - J$, of 4.0 and 5.0 eV were used for Mn- d and Fe- d orbitals, respectively.

RESULTS AND DISCUSSION

Crystal Structure. The XRPD patterns of the polycrystalline Cu_2TSiS_4 ($T = \text{Mn}$ and Fe) samples prepared via high-temperature solid-state synthesis match the theoretical patterns calculated from the polar structure in the space group $Pmn2_1$ (Figure S1). The crystal structure of Cu_2TSiS_4 ($T = \text{Mn}$ and Fe) is a cation-ordered, orthorhombic superstructure of the wurtzite structure. The wurtzite (ZnS) structure is built from the hexagonal closest packing of S ions, where the metal ions occupy half of the tetrahedral holes. In this structure, all cations are tetrahedrally coordinated by sulfide anions, and vice versa. As shown in the crystal structure of $\text{Cu}_2\text{MnSiS}_4$, the CuS_4 tetrahedra are connected via corner-sharing along the crystallographic a axis and form CuS_4 columns that are connected in a zigzag fashion along the crystallographic c axis

(Figure 1a). Similarly, MnS_4 and SiS_4 are mixed alternately to form zigzag layers between the CuS_4 layers along the b axis.

The refinements of the crystal structure of Cu_2TSiS_4 ($T = \text{Mn}$ and Fe) were carried out using the NPD data collected at 90 and 100 K, respectively. The reported polar crystal structure of Cu_2TSiS_4 ($T = \text{Mn}$ and Fe) in the space group $Pmn2_1$ was used as the initial model during the Rietveld refinements. However, it became apparent that a relatively small amount of other phases were detected in the $\text{Cu}_2\text{MnSiS}_4$ sample. Therefore, additional materials were added to the model. The final refinement indicated that $\text{Cu}_2\text{MnSiS}_4$ was the major phase (mass % = 96.7%), although small amounts of unwanted Mn_5Si_3 (mass % = 1.92%) and Cu_2SiS_3 (mass % = 1.38%) existed in the sample (Figure 2a). A peak near 5.9 Å was excluded because its intensity mainly stems from the magnetic contribution from the Mn_5Si_3 impurity phase, which orders antiferromagnetically with $T_N \sim 100$ K.³¹ The $\text{Cu}_2\text{FeSiS}_4$ sample was assessed as being phase pure, as the NPD data at 100 K could be completely accounted for with the single $\text{Cu}_2\text{FeSiS}_4$ phase (Figure 2b).

Selected refinement parameters and fractional atomic coordinates are given in Table 1. The refined unit cell parameters of $\text{Cu}_2\text{MnSiS}_4$ at 90 K are slightly smaller than those refined using room-temperature single-crystal X-ray diffraction data [$a = 7.5431(1)$ Å, $b = 6.4401(1)$ Å, $c = 6.1877(1)$ Å, and $V = 300.229(8)$ Å³] and previously reported values for $\text{Cu}_2\text{MnSiS}_4$ at 293 K [$a = 7.543(2)$ Å, $b = 6.446(1)$ Å, $c = 6.193(1)$ Å, and $V = 301.1(1)$ Å³].²⁰ The refined unit cell parameters of $\text{Cu}_2\text{FeSiS}_4$ at 100 K are also close to those refined using room-temperature single-crystal X-ray diffraction data [$a = 7.4162(1)$ Å, $b = 6.4121(1)$ Å, $c = 6.1397(1)$ Å, and

Table 1. Selected Structure Parameters and Refinement Details for Cu₂TSiSi₄ (T = Mn and Fe) Using NPD Data

nominal composition refined formula	Cu ₂ MnSiSi ₄		Cu ₂ FeSiSi ₄	
	90 K	2 K	100 K	2 K
temperature	338.38		339.28	
mol. wt./mol	3.759		3.872	
density, g/cm ³ (calculated)		3.760		3.875
space group, #	<i>Pmmn</i> 2 ₁ , # 21		<i>Pmmn</i> 2 ₁ , # 21	
<i>Z</i>	2		2	
lattice parameters	<i>a</i> = 7.5264(1) Å, <i>b</i> = 6.4250(1) Å, <i>c</i> = 6.1823(1) Å, <i>V</i> = 298.957(1) Å ³	<i>a</i> = 7.5262(2) Å, <i>b</i> = 6.4237(1) Å, <i>c</i> = 6.1817(1) Å, <i>V</i> = 298.86(1) Å ³	<i>a</i> = 7.4119(1) Å, <i>b</i> = 6.3985(1) Å, <i>c</i> = 6.1352(1) Å, <i>V</i> = 290.964(8) Å ³	<i>a</i> = 7.4115(1) Å, <i>b</i> = 6.3965(6) Å, <i>c</i> = 6.13509(8) Å, <i>V</i> = 290.854(7) Å ³
Rietveld criteria of fit of the major nuclear phase	<i>R</i> _p = 3.98%, <i>R</i> _{wp} = 3.17%, <i>R</i> _{exp} = 1.82%, <i>χ</i> ² = 3.04	<i>R</i> _p = 5.17%, <i>R</i> _{wp} = 4.44%, <i>R</i> _{exp} = 1.32%, <i>χ</i> ² = 11.3	<i>R</i> _p = 3.27%, <i>R</i> _{wp} = 2.65%, <i>R</i> _{exp} = 1.48%, <i>χ</i> ² = 3.21	<i>R</i> _p = 3.23%, <i>R</i> _{wp} = 3.44%, <i>R</i> _{exp} = 0.9%, <i>χ</i> ² = 14.6
site	Wyckoff symbol	<i>x</i> , <i>y</i> , <i>z</i>	<i>x</i> , <i>y</i> , <i>z</i>	<i>x</i> , <i>y</i> , <i>z</i>
Cu	4b	0.7528(2), 0.6781(2), 0.178(1)	0.2476(2), 0.3248(3), 0.013(2)	0.2476(2), 0.3257(3), 0.012(2)
Mn (Fe)	2a	0, 0.8441(7), 0.670(3)	0, 0.1541(3), 0.500(3)	0, 0.1548(3), 0.499(2)
Si	2a	0, 0.1748(7), 0.178(3)	0, 0.8298(8), 0	0, 0.8300(7), 0
S1	2a	0, 0.858(1), 0.062(1)	0, 0.814(1), 0.350(2)	0, 0.816(1), 0.349(2)
S2	2a	0, 0.183(1), 0.515(1)	0, 0.141(1), 0.885(2)	0, 0.141(1), 0.883(2)
S3	4b	0.7304(6), 0.6668(9), 0.550(1)	0.2643(8), 0.329(1), 0.388(1)	0.2651(8), 0.329(1), 0.388(1)

$V = 291.964(8) \text{ \AA}^3$], and published values for Cu₂FeSiSi₄ at 293 K ($a = 7.404 \text{ \AA}$, $b = 6.411 \text{ \AA}$, $c = 6.14 \text{ \AA}$, and $V = 291.45 \text{ \AA}^3$).¹² The unit cell volume of Cu₂MnSiSi₄ is slightly larger than that of Cu₂FeSiSi₄, which is because the ionic radius of the Mn²⁺ ion (0.66 Å) is larger than that of the Fe²⁺ ion (0.63 Å).³²

As shown in Figure 1, the crystal structure of Cu₂TSiSi₄ (T = Mn and Fe) consists of CuS₄, TS₄ (T = Mn and Fe), and SiS₄ tetrahedra. In each tetrahedron, Cu/Mn/Fe/Si coordinates with one S1 atom, one S2 atom, and two S3 atoms, with slightly different bond distances (*d*) within the respective tetrahedra (Table 2). The refined *d*(Cu–S) and *d*(Si–S) in the

Table 2. Selected Bond Distances in Cu₂TSiSi₄ (T = Mn and Fe) Refined at 90 and 100 K, Respectively

	Cu ₂ MnSiSi ₄		Cu ₂ FeSiSi ₄	
	Cu/Mn/Si–S distances (Å)		Cu/Fe/Si–S distances (Å)	
Cu–S1	2.304(6)		Cu–S1	2.300(8)
Cu–S2	2.333(4)		Cu–S2	2.318(9)
Cu–S3	2.31(1)		Cu–S3	2.31(1)
Cu–S3	2.356(7)		Cu–S3	2.342(8)
Mn–S1	2.43(2)		Fe–S1	2.361(1)
Mn–S2	2.377(9)		Fe–S2	2.364(2)
Mn–S3 (×2)	2.440(8)		Fe–S3 (×2)	2.359(7)
Si–S1	2.16(1)		Si–S1	2.15(1)
Si–S2	2.08(2)		Si–S2	2.11(1)
Si–S3 (×2)	2.158(9)		Si–S3 (×2)	2.135(7)

two Cu₂TSiSi₄ (T = Mn and Fe) compounds are very close in most instances or identical in some instances, considering the estimated standard deviations. As expected, *d*(Mn–S) is longer than *d*(Fe–S). The refined *d*(Cu–S) = 2.30–2.36 Å and *d*(Mn–S) = 2.38–2.44 Å are very close to those found in the isostructural Cu₂MnGeSi₄ compound [*d*(Cu–S) = 2.31–2.35 Å and *d*(Mn–S) = 2.43–2.46 Å].²⁰ The obtained *d*(Si–S) = 2.08–2.16 Å is in good agreement with the *d*(Si–S) = 2.14 Å observed in Cu₂CoSiSi₄ with the space group *I42m*.¹² Because there are four different bond distances in the CuS₄ tetrahedron and three unequal bond distances in MnS₄, FeS₄, and SiS₄ tetrahedra, all of the tetrahedra are distorted, and the chains of corner-sharing tetrahedra are unsymmetrical, as shown in Figure 1a. When looking at the projection along the crystallographic *c* axis, all atoms are connected in distorted hexagonal patterns, that is, honeycomb patterns containing three sulfide anions and three metal cations (Figure 1b). Such an arrangement of connected, distorted tetrahedra explains the polar crystal structure, and the more distorted CuS₄ tetrahedron contributes most to the polarization.

Electron Diffraction. To confirm the refined crystal structure of Cu₂TSiSi₄ (T = Mn and Fe) obtained from NPD, TEM experiments were performed. An SAED pattern of the Cu₂MnSiSi₄ sample was obtained along the [100] direction. It is consistent with the simulated pattern of Cu₂MnSiSi₄ with the space group *Pmmn*2₁. The (010) diffraction spot has a similar intensity as the (020) spot, and the extinct (001) spot has intensity due to the double diffraction, which is a typical phenomenon of the dynamical scattering of a thick crystal. The corresponding atomic resolution HAADF-STEM image shows rows of alternate bright and weak spots and a neighboring row of weaker spots. Because the atomic column image intensity in the HAADF-STEM image is almost proportional to the atomic number (*Z*²) of an atom and the number of that atom along the column, the heavier the atom, the brighter the spots.

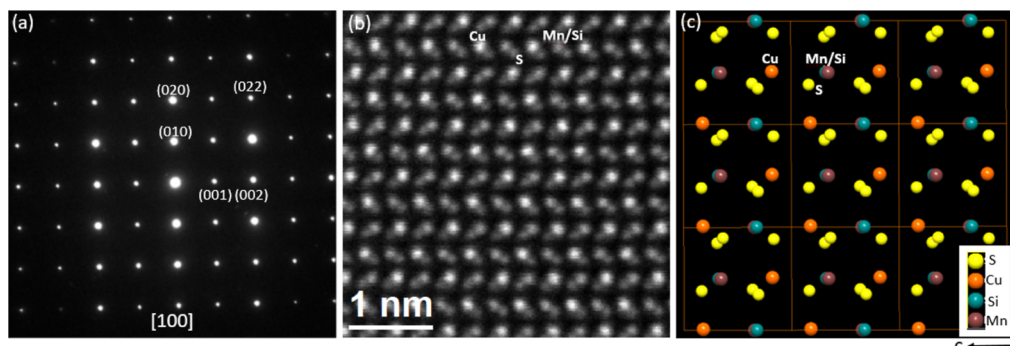


Figure 3. (a) Electron diffraction pattern along the $[100]$ direction, (b) atomic resolution HAADF-STEM image, and (c) perspective view of the crystal structure of $\text{Cu}_2\text{MnSiS}_4$ with the space group $Pmn2_1$.

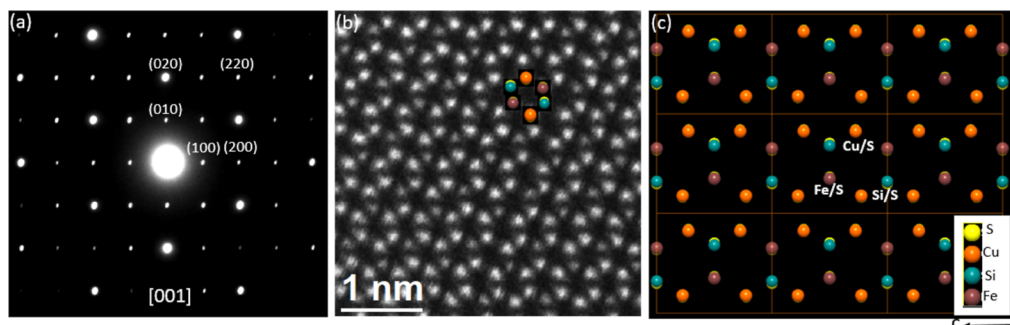


Figure 4. (a) Electron diffraction pattern along the $[001]$ direction, (b) atomic resolution HAADF-STEM image, and (c) perspective view of the crystal structure of $\text{Cu}_2\text{FeSiS}_4$ with the space group $Pmn2_1$.

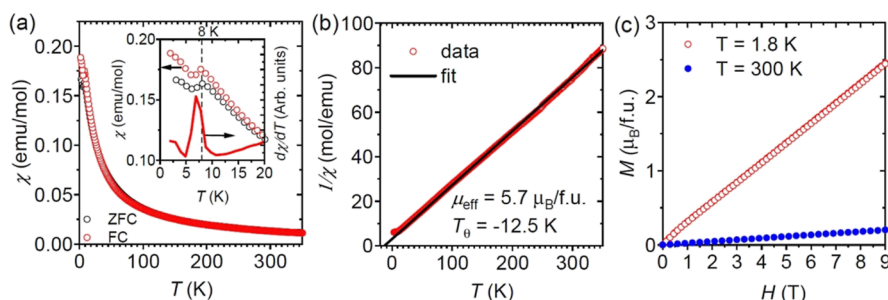


Figure 5. (a) Temperature-dependent ZFC–FC magnetic susceptibility at 0.1 T. Inset depicts the magnetic susceptibility data below 20 K (left axis) and the temperature derivative of the magnetic susceptibility (right axis), highlighting the kink that represents the magnetic phase transition. The dashed line is the guide to the eye for 8 K. (b) Inverse magnetic susceptibility fit with the Curie–Weiss law, and (c) field-dependent magnetization of polycrystalline $\text{Cu}_2\text{MnSiS}_4$.

Therefore, the intensity of Cu ($Z = 29$) is the brightest, the mixed columns of Mn ($Z = 25$) and Si ($Z = 14$) have an average atomic number of 19.5 and are less bright, and S columns ($Z = 16$) are the weakest. In Figure 3b, rows with alternate bright and weak spots are the rows of Cu atoms and Si/Mn atoms in the crystal structure of $\text{Cu}_2\text{MnSiS}_4$ with the space group $Pmn2_1$ (Figure 3c). The adjacent rows with weaker spots in Figure 3b correspond to the S atoms in the crystal structure (Figure 3c).

The electron diffraction pattern recorded from a single piece of $\text{Cu}_2\text{FeSiS}_4$ can be indexed to the $[001]$ direction with the space group $Pmn2_1$ (Figure 4a). The extinct (100) spot that has intensity is due to double diffraction. The corresponding atomic resolution HAADF-STEM image shows a pattern consisting of hexagonal spots, which correspond well with the crystal structure viewed along the $[001]$ direction (Figure 4b,c). Along this projected direction, all atomic columns are

mixed with S. Therefore, the average atomic number for Cu/S is 22.5, 21 for the Fe/S mixed column, and 15 for Si/S columns. The atomic number difference between Cu/S and Fe/S is 1.5, which is too small to have an intensity difference. Therefore, these columns should have similar bright intensities. However, Si/S should be easily identifiable with weak intensity. Therefore, the rows of bright spots with the same intensity represent the atomic Cu/S columns, and the neighboring rows with alternating weak and strong spots correspond to the rows of Si/S and Fe/S atoms. A HAADF-STEM image was also collected along the $[100]$ direction; it shows alternating bright and dim spots, indicating the ordering of Fe/Si and Cu, similar to that observed for the $\text{Cu}_2\text{MnSiS}_4$ crystal.

However, for some crystals, the electron diffraction indicates the absence of (010) reflection, and the HAADF-STEM image shows rows of spots with the same intensity, indicating the disorder of Cu with Fe/Si in the crystal structure (Figure S2).

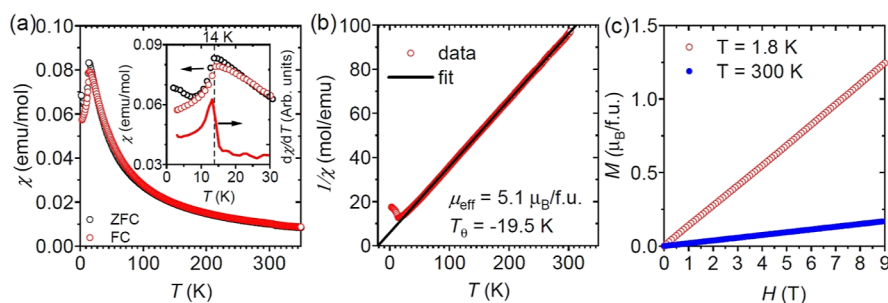


Figure 6. (a) Temperature-dependent ZFC–FC magnetic susceptibility at 0.1 T. Inset depicts the susceptibility data below 30 K (left axis) and the temperature derivative of the magnetic susceptibility (right axis), highlighting the kink that represents the magnetic phase transition. The dashed line is the guide to the eye for 14 K. (b) Inverse magnetic susceptibility fit with the Curie–Weiss law, and (c) field-dependent magnetization of polycrystalline Cu_2FeSi_4 .

The possible disorder structure might be similar to that of $\text{Cu}_2\text{CoGeSe}_4$ with the $F222$ space group, in which Cu, Co, and Ge are disordered and occupy the $4a$ (0, 0, 0) site in the crystal structure.¹² Another disordered crystal structure in the CTMS-related system is $\text{Cu}_2\text{NiSnSe}_4$ ($F\bar{4}3m$), with Cu, Ni, and Sn atoms also occupying $4a$ (0, 0, 0), the same as the above site.¹² The XRPD of this possible disordered structure is different from the polar crystal structure of $Pmn2_1$, and the corresponding peaks are not present in our patterns, indicating that the amount of such a disordered sample is too small to be detected in our X-ray or neutron powder patterns. The magnetic and optical properties should not be measurably affected by these small inclusions.

Chemical Analysis. Semiquantitative SEM–EDX measurements were performed on Cu_2TMSi_4 ($T = \text{Mn}$ and Fe) crystals. The EDX maps of the selected area ($\sim 100 \mu\text{m} \times 100 \mu\text{m}$) of the surface of the crystal indicate that the Cu, Mn, Si, and S elements are homogeneously distributed (Figure S3). The calculated molar ratio of Cu/Mn:Si/S is 1.93:1.108:4.29, which is close to the expected 2:1:1:4 ratio. Similar homogeneous distribution of Cu, Fe, Si, and S elements is also observed in the Cu_2FeSi_4 crystal with the obtained molar ratio of Cu/Mn/Fe/S = 1.95:1.102:4.08 (Figure S4).

Magnetic Properties. ZFC–FC magnetic measurements on polycrystalline Cu_2MnSi_4 and Cu_2FeSi_4 samples show AFM ordering at 8 (Figure 5a) and 14 K (Figure 6a), respectively, which are consistent with the reported values (8 and 15 K), as shown in Table 3.¹⁶ The Curie–Weiss ($\chi = C/(T - T_\theta)$) fitting of the inverse magnetic susceptibility gives a negative Weiss constant $T_\theta = -12.5$ (Figure 5b) and -19.5 K (Figure 6b) for Cu_2MnSi_4 and Cu_2FeSi_4 , respectively, indicating AFM coupling between Mn/Fe moments. The $\mu_{\text{eff}}(\text{Mn}^{2+})$ obtained from the Curie–Weiss fitting of Cu_2MnSi_4 data is $5.7 \mu_{\text{B}}$, which is also close to the theoretical value of $\mu_{\text{eff}}(\text{Mn}^{2+}) = 5.92 \mu_{\text{B}}$ and the reported values ($\mu_{\text{eff}} = 5.9 \mu_{\text{B}}$, $T_\theta = -17$ K) for Cu_2MnSi_4 .³³ The $\mu_{\text{eff}}(\text{Fe})$ obtained from the Curie–Weiss fitting of Cu_2FeSi_4 data is $5.13 \mu_{\text{B}}$, which is close to the theoretical value of $\mu_{\text{eff}}(\text{Fe}^{2+}) = 4.9 \mu_{\text{B}}$. The linear behavior of field-dependent magnetization (Figures 5c and 6c) at 1.8 K also confirms the AFM ordering in both compounds. The AFM ordering with low T_{N} has also been observed in other Cu_2TMS_4 ($T = \text{Mn}$, Fe , Co , and Ni ; $\text{M} = \text{Si}$, Ge , and Sn), as shown in Table 3.

Neutron Diffraction. Among the reported compounds of the CTMS family, only $\text{Cu}_2\text{MnGeS}_4$, $\text{Cu}_2\text{MnSnS}_4$, and $\text{Cu}_2\text{FeGeS}_4$ have had their magnetic structures investigated (Table 3).^{13,15} To determine the magnetic structures of

Table 3. Summary of Magnetic Properties of Cu_2TMS_4 ($T = \text{Mn}$, Fe , Co , and Ni ; $\text{M} = \text{Si}$, Ge , and Sn)

Compound	space group	T_{N} , K	k vector	magnetic space group	refs
Cu_2MnSi_4	$Pmn2_1$	8, 8 ^a	(1/2,0,1/2)	P_4c^a	16, 33
Cu_2FeSi_4	$Pmn2_1$	15, 14 ^a	(1/2,1/2,1/2) ^a	C_4c^a	12, 16
Cu_2CoSi_4	$\bar{I}42m$				34
Cu_2NiSi_4					
$\text{Cu}_2\text{MnGeS}_4$	$Pmn2_1$	8.3, 9	(1/2,0,1/2)	P_4c	13, 16, 20, 35, 36
$\text{Cu}_2\text{FeGeS}_4$	$\bar{I}42m$	12, 17	(1/2,0,1/2)		12, 15, 16, 33
$\text{Cu}_2\text{CoGeS}_4$	$\bar{I}42m$	25			33, 34
$\text{Cu}_2\text{NiGeS}_4$	$\bar{I}42m, \bar{I}4$	36			33, 37, 38
$\text{Cu}_2\text{MnSnS}_4$	$\bar{I}42m$	8.8, 10	(1/2,0,1/2)	P_22_1	13, 14, 16, 20, 39
$\text{Cu}_2\text{FeSnS}_4$ (β)	$\bar{I}42m$	6.1, 7, 8			9, 40–42
$\text{Cu}_2\text{FeSnS}_4$ (α)	$\bar{P}4$	38			11, 43
$\text{Cu}_2\text{CoSnS}_4$	$\bar{I}42m$				34
$\text{Cu}_2\text{NiSnS}_4$	$F\bar{4}3m$				12

^aThis work.

Cu_2MnSi_4 and Cu_2FeSi_4 , NPD measurements were performed between 90–2 K and 100–2 K, respectively. Selected NPD patterns are shown in Figure 7. For the Cu_2MnSi_4 sample, the pattern remains the same as the temperature decreases from 90 to 7.5 K, but new magnetic reflections show up below approximately 7.5 K, and their intensities increase as the temperature decreases. The observation of magnetic reflections at 7 K confirms the AFM transition determined by the magnetic measurements (Figure 5a). By comparison of the NPD patterns of 90 and 2 K (Figure S5), the obvious six magnetic reflections appearing at a lower temperature can be identified at 9.3, 5.3, 4.65, 3.97, 3.38, and 3.04 Å. For the Cu_2FeSi_4 sample, new magnetic reflections appear below 14 K, which also supports the AFM ordering observed in the magnetic data (Figure 6a). The intensity of magnetic reflections increases as the temperature decreases to 2 K (Figure 7b). There are eight obvious peaks attributed to the magnetic structure being located at 7.6, 4.31, 3.89, 3.77, 3.12, 2.89, 2.54, and 2.47 Å (Figures 7b and S5).

In the NPD data of Cu_2MnSi_4 collected at 2 K, the observed magnetic peaks can be indexed using the magnetic propagation vector $k = (1/2, 0, 1/2)$, with the most intense peak (1/2, 0, 1/2) located at 9.3 Å. The nuclear peaks observed at 2

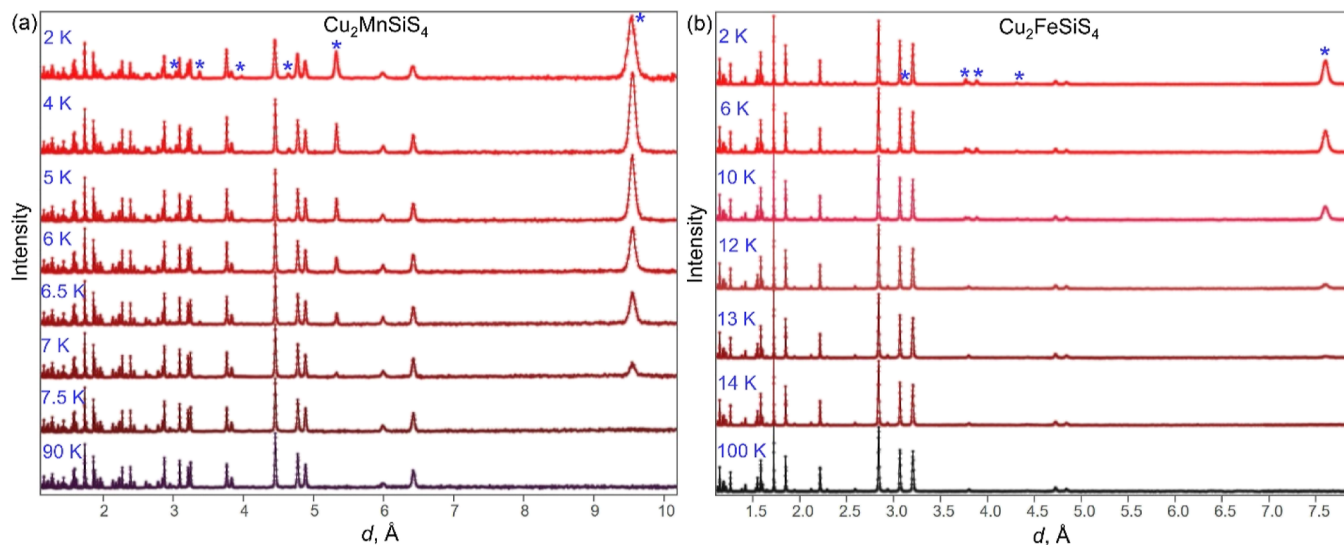


Figure 7. (a) Selected NPD patterns of $\text{Cu}_2\text{MnSiS}_4$ between 90 and 2 K and (b) $\text{Cu}_2\text{FeSiS}_4$ between 100 and 2 K. Magnetic peaks are marked with a star (*) symbol. For clarity purposes, only a few of the strongest peaks are marked.

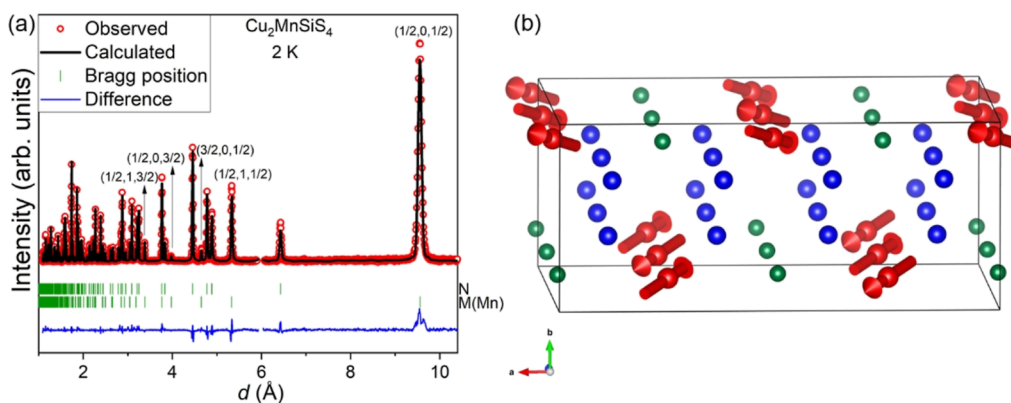


Figure 8. (a) Rietveld refinement of $\text{Cu}_2\text{MnSiS}_4$ (space group $Pmn2_1$) using NPD data (2 K) with observed data (red), the calculated pattern (black), difference between the observed and calculated patterns (blue), and Bragg peak positions of major nuclear and magnetic reflections (green). (b) Magnetic structure of $\text{Cu}_2\text{MnSiS}_4$ (color code: Cu = blue, Mn = red, and Si = green; S atoms are omitted for clarity).

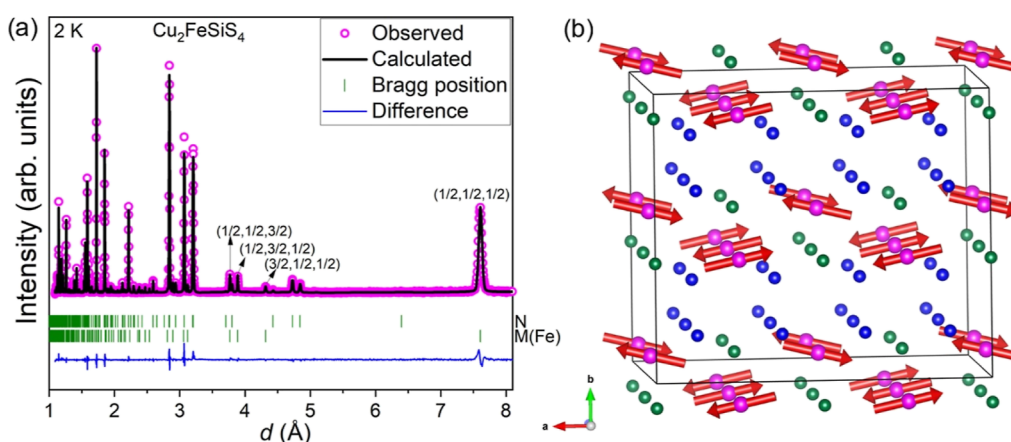


Figure 9. (a) Rietveld refinement of $\text{Cu}_2\text{FeSiS}_4$ (space group $Pmn2_1$) using NPD (2 K) data, with observed data (red), the calculated pattern (black), the difference between the observed and calculated patterns (blue), and Bragg peak positions of nuclear and magnetic reflections (green). (b) Magnetic structure of $\text{Cu}_2\text{FeSiS}_4$ (color code: Cu = blue, Fe = magenta, and Si = green, and S atoms are omitted for clarity).

K can be fit well with the same nuclear structure model used for the 90 K data set (Figure 8a). The refined unit cell parameters and atomic positions show a very small difference between the two temperatures (Table 1). The only magnetic

ions in the unit cell are Mn^{2+} ions, occupying only one Wyckoff position, $2a$. The best-fitting magnetic structure model involves an alignment of Mn magnetic moments along the MnS_4 tetrahedral edge, with the Mn pair inside the chemical unit

cell having the m_a and m_c components parallel but the m_b components antiparallel to each other. The moments are alternating their directions along the a and c directions, resulting in an overall antiferromagnetic structure. The determined magnetic structure is shown in Figure 8b, with the magnetic unit cell doubled in a and c directions as compared to the nuclear structure. This magnetic structure adopts the magnetic space group $P_{21}c$ (#7.27).²³ The refined magnetic components of Mn at 2 K are $m_a = 2.25(5) \mu_B$, $m_b = 1.0(1) \mu_B$, and $m_c = -3.18(5) \mu_B$, which yield a total magnetic moment m_{Mn} of $4.1(1) \mu_B$. The canting angle away from the ac plane is about 14° . Other refined parameters of the magnetic structure are given in Table S4.

This magnetic propagation vector of $\text{Cu}_2\text{MnSiS}_4$ is the same as that of isostructural $\text{Cu}_2\text{MnGeS}_4$ and stannite $\text{Cu}_2\text{MnSnS}_4$ (space group $I42m$),^{13,14} and the refined magnetic moment ($4.1 \mu_B$) for $\text{Cu}_2\text{MnSiS}_4$ is just slightly smaller than that obtained for other compounds: $\sim 4.3 \mu_B$ ($\text{Cu}_2\text{MnGeS}_4$) and $\sim 4.28 \mu_B$ ($\text{Cu}_2\text{MnSnS}_4$).^{13,14} The isostructural $\text{Cu}_2\text{MnGeS}_4$ has been reported to be ordered with the same magnetic space group symmetry $P_{21}c$, but the moments are rotated from the c direction toward the b axis ($m_a \approx 2.6 \mu_B$, $m_b = 3.3 \mu_B$, and $m_c = 0.9 \mu_B$).¹³ $\text{Cu}_2\text{MnSnS}_4$ exhibits a collinear AFM magnetic structure (magnetic space group $P_{21}c$) with $k = (1/2, 0, 1/2)$, in which the magnetic moments are constrained by symmetry to lie in the ac plane ($m_b = 0 \mu_B$). Nevertheless, the moments are still mainly oriented toward the edge of the MnS_4 tetrahedra, with a small deviation of $11 \pm 5^\circ$ away from the crystallographic c axis.¹⁴

The magnetic peaks that appear in the low-temperature ($T < 14$ K) NPD data of $\text{Cu}_2\text{FeSiS}_4$ can be indexed by the wave vector $k = (1/2, 1/2, 1/2)$. The nuclear contribution to the NPD data collected at 2 K can be fit well using the same structural model as that used for the refinement using the data obtained at 100 K (Figure 9a). The refined unit cell parameter and atomic positions almost remained the same. The determined magnetic structure model that accounts well for all magnetic intensities is displayed in Figure 9b. Similar to $\text{Cu}_2\text{MnSiS}_4$, the two equivalent sites of the nuclear cell [(Fe^{2+} located at (0, 0.155, 0.509) and (0.5, 0.845, 0.009)] have parallel m_a and m_c components but antiparallel m_b . The magnetic moments alternate their directions along all three crystallographic directions, leading to a magnetic unit cell eight times larger than the nuclear lattice. The corresponding magnetic space group is C_{2c} (#9.41). The refined magnetic components of Fe at 2 K are $m_a = 2.85(3) \mu_B$, $m_b = 0.7(1) \mu_B$, and $m_c = 0.5(1) \mu_B$, which yields a total magnetic moment of $2.9(1) \mu_B$. The spin axis is oriented at about 14° from the ac plane, which is very similar to the canting determined for the Mn congener. Other refined parameters of the magnetic structure are given in Table S5.

The determined magnetic structures for both investigated compounds can be viewed as consisting of chains of collinear spins that are arranged antiferromagnetically along the c direction. The magnetic moments of adjacent chains are canted with respect to each other around the b axis. While in the Mn compound, the direction of the spins only alternates inside the chain (c axis) and along the a axis; in the $\text{Cu}_2\text{FeSiS}_4$ compound, the Fe spins are alternating their orientation in all crystallographic directions. A propagation vector $k = (1/2, 0, 1/2)$ has been observed for all studied Mn systems [$\text{Cu}_2\text{MnSiS}_4$, $\text{Cu}_2\text{MnGeS}_4$, $\text{Cu}_2\text{MnSnS}_4$ (space group $I42m$)] and also for $\text{Cu}_2\text{FeGeS}_4$ (space group $I42m$).^{13–15} In the latter, four

distinct magnetic structure models compatible with the propagation vector $k = (1/2, 0, 1/2)$ have been discussed, but the final model has not been determined.¹⁵ The magnetic structure of the other related Fe-containing sulfide, $\text{Cu}_2\text{FeSnS}_4$, has not been reported. Considering selenides and tellurides as well, $\text{Cu}_2\text{FeGeS}_4$ is the first example with a $k = (1/2, 1/2, 1/2)$ magnetic order in the quaternary Cu_2FeMX_4 ($M = \text{Si, Ge, and Sn}$; $X = \text{S, Se, and Te}$) chalcogenide family. The propagation vector $k = (1/2, 1/2, 1/2)$ and a similar magnetic moment of Fe ($2.82 \mu_B$) have also been observed in the related $\text{Li}_2\text{FeGeS}_4$, a polar (space group Pn) antiferromagnet ($T_N \sim 6$ K) with collinear magnetic Fe spins along the b axis, which is different from the incommensurate [$k = (0, 0, 0.546)$] collinear magnetic structure in the polar (space group Pn) antiferromagnet ($T_N \sim 4$ K) $\text{Li}_2\text{FeGeS}_4$.⁴⁴

Attenuated Total Reflectance–Fourier Transform Infrared Spectroscopy. ATR–FT–IR spectroscopy was used to assess the windows of optical clarity for Cu_2TSiS_4 ($T = \text{Mn and Fe}$). Accurate and extreme transparency necessary for NLO devices should be determined using high-quality single-crystal specimens, but ATR–FT–IR of microcrystalline samples provides a general idea of the transparency. As expected for sulfides, the IR transparency is very high, with both compounds exhibiting values above 80% transparency throughout the entire measured range of 2.5 to $25 \mu\text{m}$ (Figure S6).

Second-Order NLO Property Measurements. Using an incident wavelength of $\lambda = 1800$ nm, the SHG dependence on the particle size was investigated for the title compounds and compared to that of the NLO reference materials. The AGS reference exhibits a clear phase-matching (PM) trend, as indicated by increasing SHG counts with increasing particle size. This result is consistent with the known PM onset, which is indeed $\lambda = 1800$ nm for AGS. On the other hand, the SHG response of the title compounds does not increase with increasing particle size, signifying that they are non-phase-matching (NPM) at this wavelength. Normally, broadband NLO studies would be performed to search for a possible PM onset, as most related compounds that have been studied are PM at some longer wavelengths; however, this was not possible for the title compounds. The Cu_2TSiS_4 ($T = \text{Mn and Fe}$) samples did not exhibit enough SHG counts in the mid-IR, $\lambda > 2400$ nm to be detected with an InGaAs detector, and they did not have a measurable response for $\lambda = 1064$ nm either. Therefore, the SHG coefficients of the title compounds were assessed by comparing them with the SHG counts from AGSe, which is also NPM at $\lambda = 1800$ nm.

It should be noted that because the title compounds did not exhibit a measurable SHG response at $\lambda = 1064$ nm, the laser-induced damage thresholds (LIDTs), which are almost always reported for $\lambda = 1064$ nm, could not be assessed. However, given the relatively narrow optical band gaps of the title compounds, outstanding LIDTs are not anticipated.

The second-order NLO susceptibility of each sample, $\chi_S^{(2)}$, was calculated by comparing it with that of AGSe using the Kurtz powder method for the NPM case;⁴⁵ where I_S^{SHG} and I_R^{SHG} are the experimentally measured SHG counts from the test sample and the reference, respectively.

$$\chi_S^{(2)} = \chi_R^{(2)} \frac{I_R}{I_S} \left(\frac{I_S^{\text{SHG}}}{I_R^{\text{SHG}}} \right)^{1/2} \quad (1)$$

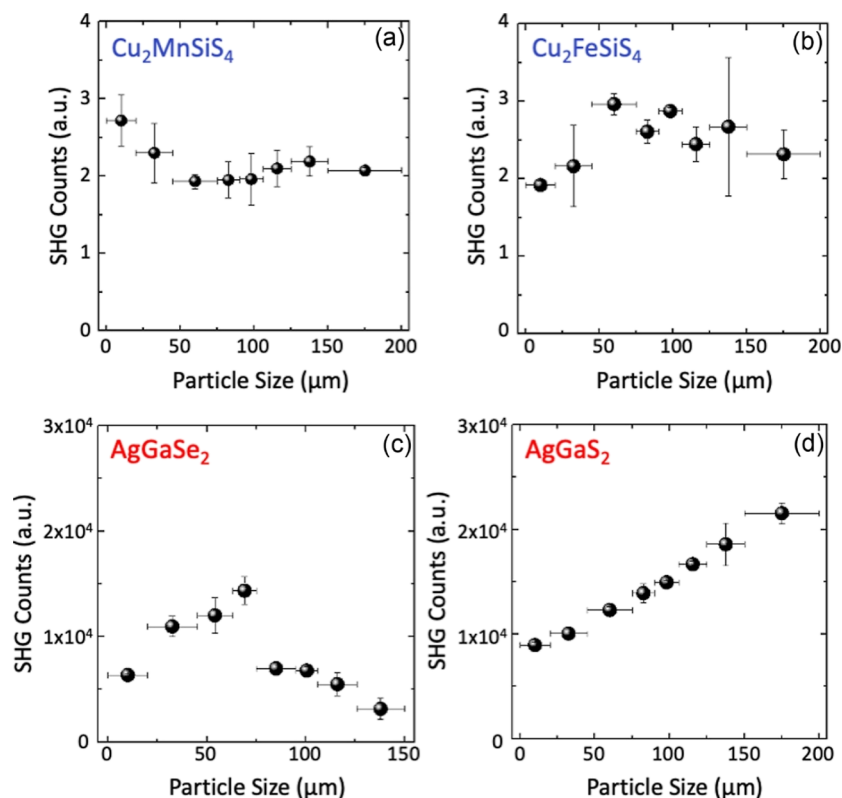


Figure 10. Particle size dependence of the SHG response for (a) Cu_2MnSi_4 and (b) Cu_2FeSi_4 compared to that of the (c) AGSe and (d) AGS reference materials. At this incident wavelength, $\lambda = 1800$ nm (i.e., $\lambda_{\text{SHG}} = 900$ nm), only the AGS is phase matchable.

In eq 1, l_S and l_R are the experimentally measured coherence lengths that correspond to the maximum SHG counts in Figure 10. Using $\chi_S^{(2)} \sim 66$ pm/V for AGSe,⁴⁶ our calculation yields $\chi_S^{(2)}$ (Cu_2MnSi_4) $\sim 6.27 \pm 0.07$ pm/V and $\chi_S^{(2)}$ (Cu_2FeSi_4) $\sim 1.09 \pm 0.03$ pm/V, respectively. Although both compounds exhibit rather similar SHG counts, the difference in $\chi_S^{(2)}$ arises from the difference in the coherence lengths. While both title compounds definitely yield a finite SHG response, the SHG intensities are quite weak compared with AGSe and AGS ($\chi_R^{(2)} \sim 36$ pm/V) (b),⁴⁷ which are benchmark IR-NLO materials, and the resulting $\chi_S^{(2)}$ values are expectedly modest.

To put things into perspective, one can consider these results for the title compounds in the context of other quaternary chalcogenides with the same or similar crystal structures. Although the nonpolar $\text{Cu}_2\text{ZnGeSe}_4$ (space group $I\bar{4}$) with the kesterite structure has a similar band gap (1.38 eV) to Cu_2MnSi_4 (theoretical $E_g^{\text{direct}} = 1.73$ eV as shown in Figure 12), it has a much better SHG performance with $\chi_S^{(2)} \sim 43$ pm/V.⁴⁸ On the other hand, the polar $\text{Cu}_4\text{ZnGe}_2\text{Se}_7$ (space group $C2$), which has a more complex superstructure of zinc blend and a narrower optical band gap (0.91 eV), only exhibited a very weak SHG response, such that the $\chi_S^{(2)}$ value was not determined.⁴⁸ The polar $\text{Li}_2\text{MnGeS}_4$ (space group $Pna2_1$) with a different superstructure of the W structure demonstrates a similar SHG efficiency as Cu_2MnSi_4 , $\chi_S^{(2)} \sim 6.6$ pm/V, although the optical band gap of the former is much wider (3.07 eV).⁴⁹ Some other compounds with the same WST structure as the title compounds, such as $\text{Cu}_2\text{MnGeS}_4$ and $\text{Li}_2\text{CdGeS}_4$, not only have much stronger SHG responses with $\chi_S^{(2)} \sim 16.9$ pm/V and $\chi_S^{(2)} \sim 22.5$ pm/V but also possess considerably larger optical band gaps of 2.21 and 3.15 eV,

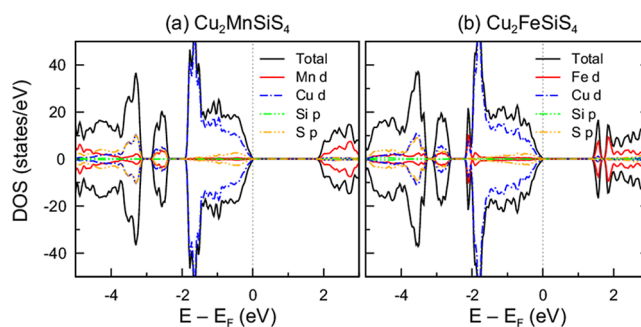


Figure 11. Total and partial densities of states (DOS) of (a) Cu_2MnSi_4 and (b) Cu_2FeSi_4 with collinear AFM structures. The positive and negative values in DOS correspond to spin-up and -down configurations, respectively.

respectively.^{1,18,19} In a nutshell, the performance of the title compounds lies in the same realm as related materials, which vary widely in their SHG responses and optical band gap energies.

Electronic Structure Calculations. DFT calculations were carried out to investigate the electronic structures of Cu_2MSi_4 ($M = \text{Mn}$ and Fe). From the NPD experiments, these systems show canted AFM ordering. In the spin-polarized DFT calculations, however, collinear AFM structures were used instead for both systems for simplicity. This simplification might change the details of the electronic structure but does not alter the general conclusion of this study.

DFT calculations were performed with on-site Coulomb repulsion parameters $U_{\text{eff}} = 4$ and 5 eV chosen for Cu_2MnSi_4 and Cu_2FeSi_4 , respectively. Those values are comparable to

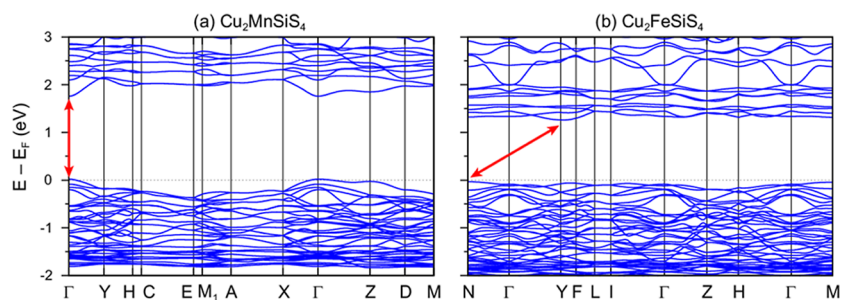


Figure 12. Band dispersions of (a) $\text{Cu}_2\text{MnSiS}_4$ and (b) $\text{Cu}_2\text{FeSiS}_4$ (b) with collinear AFM structures.

those used in previous DFT studies on similar compounds.^{50,51} The DOS for both systems with collinear AFM structures are presented in Figure 11. The DFT calculations show that both systems are semiconductors with band gaps >1 eV. The band gap is formed between the top of the valence band with mostly Cu d character and the bottom of the conduction band with mostly Mn (Fe) d character in the case of $\text{Cu}_2\text{MnSiS}_4$ ($\text{Cu}_2\text{FeSiS}_4$). The character of dominating Cu d orbitals near valence band maximum (VBM) is also observed in Cu_2MGeS_4 ($T = \text{Mn}$ and Ni) and $\text{Cu}_2\text{TnSnS}_4$ ($M = \text{Mn}$, Fe , and Ni),^{50,52–54} which is different from the character of hybridization of Cu d and S p found in Cu_2CoMS_4 ($M = \text{Ge}$, Sn).^{55,56} The feature of T d orbitals near the conduction band minimum (CBM) of Cu_2TSiS_4 ($T = \text{Mn}$ and Fe) is similar to that of Cu_2NiMS_4 ($M = \text{Ge}$ and Sn),^{38,53,54} and $\text{Cu}_2\text{CoGeS}_4$,⁵⁵ which is different from the hybridization of Mn d , Ge s , and S p in $\text{Cu}_2\text{MnGeS}_4$,⁵² Sn s and S p in $\text{Cu}_2\text{TnSnS}_4$ ($M = \text{Mn}$ and Fe),⁵⁴ and Co d and S p in $\text{Cu}_2\text{CoSnS}_4$.⁵⁶

The DFT calculations indicate that ordered magnetic moments are only realized in Mn (Fe) sites for $\text{Cu}_2\text{MnSiS}_4$ ($\text{Cu}_2\text{FeSiS}_4$). The size of the ordered magnetic moment is $4.55 \mu_B/\text{Mn}$ and $4.35 \mu_B/\text{Fe}$ for $\text{Cu}_2\text{MnSiS}_4$ and $\text{Cu}_2\text{FeSiS}_4$, respectively. Magnetic exchange interaction was also estimated within the DFT framework by computing an energy difference between the ferromagnetic (FM) and collinear AFM magnetic ordering phases, that is, $E_{\text{FM}} - E_{\text{AFM}}$. The magnitudes of the computed magnetic exchange interactions are 3.38 meV per Mn and 4.39 meV per Fe for $\text{Cu}_2\text{MnSiS}_4$ and $\text{Cu}_2\text{FeSiS}_4$, respectively.

Band structure calculations indicate that $\text{Cu}_2\text{MnSiS}_4$ is a semiconductor with a direct band gap ($E_g^{\text{direct}} = 1.73$ eV) located at Γ , while $\text{Cu}_2\text{FeSiS}_4$ has an indirect band gap ($E_g^{\text{indirect}} = 1.52$ eV) formed from N (VBM) to Y (CBM) (Figure 12). The calculated band gaps are in a reasonable range compared to those calculated for the previously reported CTMS and related compounds: $\text{Ag}_2\text{FeSiS}_4$ ($E_g^{\text{direct}} = 1.99$ eV),⁵⁷ $\text{Cu}_2\text{MnGeS}_4$ ($E_g^{\text{direct}} = 1.72$ eV),⁵² $\text{Cu}_2\text{FeGeS}_4$ ($E_g^{\text{direct}} = 1.8$ eV),⁵⁸ $\text{Cu}_2\text{CoGeS}_4$ ($E_g^{\text{direct}} = 0.81$ eV),⁵⁵ $\text{Cu}_2\text{NiGeS}_4$ ($E_g^{\text{direct}} = 1.76, 1.78$ eV),⁵³ $\text{Cu}_2\text{MnSnS}_4$ ($E_g^{\text{direct}} = 1.4, 1.52$ eV),^{54,59} $\text{Cu}_2\text{FeSnS}_4$ ($E_g^{\text{direct}} = 1.7$ eV),⁵⁴ $\text{Cu}_2\text{CoSnS}_4$ ($E_g^{\text{direct}} = 1.2$ eV),⁵⁶ and $\text{Cu}_2\text{NiSnS}_4$ ($E_g^{\text{direct}} = 1.29$ eV).⁵⁴ The indirect band gap is already reported in $\text{Ag}_2\text{MnSnS}_4$ ($E_g^{\text{indirect}} = 2.00$ eV) and $\text{Li}_2\text{FeSnS}_4$ ($E_g^{\text{indirect}} = 1.42$ eV) based on optical measurements.^{44,60}

CONCLUSIONS

Both polycrystalline and single-crystal Cu_2TSiS_4 ($T = \text{Mn}$ and Fe) have been successfully prepared and adopt the same WST polar crystal structure supported by NPD, X-ray powder and single-crystal diffraction, TEM, and SHG measurements. The

polar crystal structure also remains below 100 K based on temperature-dependent NPD experiments. Although Cu_2TSiS_4 ($T = \text{Mn}$ and Fe) adopt the same crystal structure and show similar AFM behavior at low temperatures, their magnetic structures are distinct, with different magnetic propagation vectors. Interestingly, both magnetic Mn and Fe spins are canted away from the ac plane by about the same degree. Cu_2TSiS_4 ($T = \text{Mn}$ and Fe) also show SHG responses, which fall in the same realm as related compounds, but both compounds are not PM in the region where they perform best. DFT calculations suggest the direct band gap for $\text{Cu}_2\text{MnSiS}_4$ and the indirect band gap for $\text{Cu}_2\text{FeSiS}_4$. As members of CTMS, Cu_2TSiS_4 ($T = \text{Mn}$ and Fe) compounds are polar magnetic semiconductors with NLO responses as well, which is rare in this series. The detailed study of the polar crystal structure, magnetic structure, electronic structure, optical transparency in the IR region, and NLO responses will benefit the investigation of the large family of $\text{AB}^{\text{II}}\text{M}^{\text{IV}}\text{X}_4$ ($A =$ alkali metals, Cu, and Ag; $B =$ alkaline earth metals, transitional metals, Pb, and Eu; $M =$ Si, Ge, and Sn; $X =$ O, S, Se, and Te) compounds as multifunctional magnetic semiconductors with potential applications in photovoltaic, NLO, ferroelectric, magnetoelectric, and multiferroic areas.

ASSOCIATED CONTENT

Supporting Information

The Supporting Information is available free of charge at <https://pubs.acs.org/doi/10.1021/acs.inorgchem.2c03754>.

X-ray single-crystal data collection and structure refinement parameters of Cu_2TSiS_4 ($T = \text{Mn}$ and Fe); XRPD patterns of Cu_2TSiS_4 ($T = \text{Mn}$ and Fe); electron diffraction of $\text{Cu}_2\text{FeSiS}_4$; EDX elemental maps and SEM image of Cu_2TSiS_4 ($T = \text{Mn}$ and Fe) single crystals; NPD patterns of $\text{Cu}_2\text{MnSiS}_4$ at 90 and 2 K and $\text{Cu}_2\text{FeSiS}_4$ at 100 and 2 K; and FT-IR-ATR data plotted as percent transmittance for Cu_2TSiS_4 ($T = \text{Mn}$ and Fe) (PDF)

Accession Codes

CCDC 2211728 and 2211730 contain the supplementary crystallographic data for this paper. These data can be obtained free of charge via www.ccdc.cam.ac.uk/data_request/cif, or by emailing data_request@ccdc.cam.ac.uk, or by contacting The Cambridge Crystallographic Data Centre, 12 Union Road, Cambridge CB2 1EZ, UK; fax: +44 1223 336033.

AUTHOR INFORMATION

Corresponding Authors

Joon I. Jang – Department of Physics, Sogang University, Seoul 04017, Republic of Korea; orcid.org/0000-0002-1608-8321; Email: jjcoupling@sogang.ac.kr

Xiaoyan Tan – Department of Chemistry and Biochemistry, George Mason University, Fairfax, Virginia 22030, United States; orcid.org/0000-0002-1742-8252; Email: xtan6@gmu.edu

Authors

Zachary T. Messegee – Department of Chemistry and Biochemistry, George Mason University, Fairfax, Virginia 22030, United States; orcid.org/0000-0001-9702-580X

Jun Sang Cho – Department of Physics, Sogang University, Seoul 04017, Republic of Korea

Andrew J. Craig – Department of Chemistry and Biochemistry, Duquesne University, Pittsburgh, Pennsylvania 15282, United States

V. Ovidiu Garlea – Neutron Scattering Division, Oak Ridge National Laboratory, Oak Ridge, Tennessee 37831, United States

Yan Xin – National High Magnetic Field Laboratory, Florida State University, Tallahassee, Florida 32310, United States

Chang-Jong Kang – Department of Physics, Chungnam National University, Daejeon 34134, Republic of Korea; Institute of Quantum Systems, Chungnam National University, Daejeon 34134, Republic of Korea; orcid.org/0000-0003-2895-4888

Thomas E. Proffen – Neutron Scattering Division, Oak Ridge National Laboratory, Oak Ridge, Tennessee 37831, United States; orcid.org/0000-0002-1408-6031

Hari Bhandari – Department of Physics and Astronomy, George Mason University, Fairfax, Virginia 22030, United States; Quantum Science and Engineering Center, George Mason University, Fairfax, Virginia 22030, United States

Jordan C. Kelly – Department of Chemistry and Biochemistry, Duquesne University, Pittsburgh, Pennsylvania 15282, United States; orcid.org/0000-0002-6539-9169

Nirmal J. Ghimire – Department of Physics and Astronomy, George Mason University, Fairfax, Virginia 22030, United States; Quantum Science and Engineering Center, George Mason University, Fairfax, Virginia 22030, United States; orcid.org/0000-0002-8474-4968

Jennifer A. Aitken – Department of Chemistry and Biochemistry, Duquesne University, Pittsburgh, Pennsylvania 15282, United States; orcid.org/0000-0001-8281-5091

Complete contact information is available at:

<https://pubs.acs.org/10.1021/acs.inorgchem.2c03754>

Notes

The authors declare no competing financial interest.

ACKNOWLEDGMENTS

Z.T.M. and X.T. were supported by start-up funding from George Mason University. J.A.A. and A.J.C. recognize funding provided by the United States National Science Foundation, DMR-1611198. J.I.J. acknowledges support from the Basic Science Research Programs (2021R1A2C2013625) through the National Research Foundation of Korea (NRF), funded by the Korean government. Special thanks to G&H Cleveland for donating the optical-grade AGS and AGSe reference materials

that were used for NLO studies. N.J.G. acknowledges the support from the National Science Foundation (NSF) CAREER award DMR-2143903. Magnetic measurements at Argonne National Laboratory were supported by the U.S. Department of Energy, Office of Science, Basic Energy Sciences, Materials Science and Engineering Division. C.J.K. was supported by the NRF grant (NRF-2022R1C1C1008200). This work used resources at the Spallation Neutron Source, DOE Office of Science Facilities operated by the Oak Ridge National Laboratory. TEM work was performed at the National High Magnetic Field Laboratory, which is supported by National Science Foundation Cooperative agreement no. DMR-1644779 and the State of Florida. We thank Dr. Thomas J. Emge (Rutgers, The State University of New Jersey) for helping with single-crystal refinements.

REFERENCES

- (1) Glenn, J. R.; Cho, J. B.; Wang, Y.; Craig, A. J.; Zhang, J. H.; Cribbs, M.; Stoyko, S. S.; Rosello, K. E.; Barton, C.; Bonnoni, A.; et al. $\text{Cu}_4\text{MnGe}_2\text{S}_7$ and $\text{Cu}_2\text{MnGeS}_4$: two polar thiogermanates exhibiting second harmonic generation in the infrared and structures derived from hexagonal diamond. *Dalt. Trans.* **2021**, *50*, 17524–17537.
- (2) Wang, W.; Winkler, M. T.; Gunawan, O.; Gokmen, T.; Todorov, T. K.; Zhu, Y.; Mitzi, D. B. Device Characteristics of CZTSSe Thin-Film Solar Cells with 12.6% Efficiency. *Adv. Energy Mater.* **2014**, *4*, 1301465.
- (3) Baskaran, P.; Nisha, K. D.; Harish, S.; Prabakaran, S.; Navaneethan, M.; Archana, J.; Ponnusamy, S.; Muthamizhchelvan, C.; Ikeda, H. High-performance electrocatalytic and cationic substitution in $\text{Cu}_2\text{ZnSnS}_4$ as a low-cost counter electrode for Pt-free dye-sensitized solar cells. *J. Mater. Sci.* **2021**, *56*, 4135–4150.
- (4) Sabry, N.; Zahran, H. Y.; Yousef, E. S.; Algarni, H.; Umar, A.; Albargi, H. B.; Yahia, I. S. Gamma-ray attenuation, fast neutron removal cross-section and build up factor of $\text{Cu}_2\text{MnGe}[\text{S}, \text{Se}, \text{Te}]_4$ semiconductor compounds: Novel approach. *Radiat. Phys. Chem.* **2021**, *179*, 109248.
- (5) Isacfranklin, M.; Yuvakkumar, R.; Ravi, G.; Velauthapillai, D.; Pannipara, M.; Al-Sehemi, A. G. Superior supercapacitive performance of $\text{Cu}_2\text{MnSnS}_4$ asymmetric devices. *Nanoscale Adv.* **2021**, *3*, 486–498.
- (6) Ammar, H. R.; Sivasankaran, S.; Alaboodi, A. S.; Alshataif, Y. A.; Al-Mufadi, F. A. Synthesis, phase evolutions, microstructures, and compaction behavior of four copper-chalcogenide micron-thermoelectric powders ($\text{Cu}_2\text{ZnSnS}_4/\text{Se}_{4x}$, $\text{Cu}_2\text{MnSiS}_4/\text{Se}_{4x}$, $\text{Cu}_2\text{MnSnS}_4/\text{Se}_{4x}$, and $\text{Cu}_2\text{ZnSiS}_4/\text{Se}_{4x}$) prepared by mechanical alloying. *Mater. Chem. Phys.* **2021**, *271*, 124943.
- (7) Xiao, C.; Li, K.; Zhang, J.; Tong, W.; Liu, Y.; Li, Z.; Huang, P.; Pan, B.; Su, H.; Xie, Y. Magnetic Ions in Wide Band Gap Semiconductor Nanocrystals for Optimized Thermoelectric Properties. *Mater. Horiz.* **2014**, *1*, 81–86.
- (8) Goto, Y.; Naito, F.; Sato, R.; Yoshiyasu, K.; Itoh, T.; Kamihara, Y.; Matoba, M. Enhanced Thermoelectric Figure of Merit in Stannite-Kuramite Solid Solutions $\text{Cu}_{2+x}\text{Fe}_{1-x}\text{SnS}_{4-y}$ ($x = 0-1$) with Anisotropy Lowering. *Inorg. Chem.* **2013**, *52*, 9861–9866.
- (9) Brockway, L. O. The Crystal Structure of Stannite, $\text{Cu}_2\text{FeSnS}_4$. *Z. Kristallogr.* **1934**, *89*, 434–441.
- (10) Hall, S. R.; Szymanski, J. T.; Stewart, J. M. Kesterite, $\text{Cu}_2(\text{Zn}, \text{Fe})\text{SnS}_4$, and Stannite, $\text{Cu}_2(\text{Fe}, \text{Zn})\text{SnS}_4$, Structurally Similar but Distinct Minerals. *Can. Mineral.* **1978**, *16*, 131–137.
- (11) Llanos, J.; Tapia, M.; Mujica, C.; Oro-Sole, J.; Gomez-Romero, P. A New Structural Modification of Stannite. *Bol. Soc. Chil. Quim.* **2000**, *45*, 605–609.
- (12) Schäfer, W.; Nitsche, R. Tetrahedral Quaternary Chalcogenides of the Type $\text{Cu}_2\text{-II-IV-S}_4(\text{Se}_4)$. *Mater. Res. Bull.* **1974**, *9*, 645–654.
- (13) Allemand, J.; Wintenberger, M. Étude des structures magnétiques de $\text{Cu}_2\text{MnSnS}_4$ et $\text{Cu}_2\text{MnGeS}_4$ par diffraction neutronique. *Cristallogr. Bull. la Soc. Fr. Mineral.* **1970**, *93*, 141–145.

- (14) Fries, T.; Shapira, Y.; Palacio, F.; Morón, M. C.; McIntyre, G. J.; Kershaw, R.; Wold, A.; McNiff, E. J. Magnetic ordering of the antiferromagnet $\text{Cu}_2\text{MnSnS}_4$ from magnetization and neutron-scattering measurements. *Phys. Rev. B: Condens. Matter Mater. Phys.* **1997**, *56*, 5424–5431.
- (15) Wintenberger, M. Etude de la structure cristallographique et magnetique de $\text{Cu}_2\text{FeGeS}_4$ et remarque sur la structure magnetique de $\text{Cu}_2\text{MnSnS}_4$. *Mater. Res. Bull.* **1979**, *14*, 1195–1202.
- (16) Quintero, M.; Quintero, E.; Moreno, E.; Marquina, J.; Alvarez, S.; Rincón, C. Magnetic Susceptibility for the $\text{Cu}_2\text{-II-IV-S}_4$ (II = Mn, Fe; IV = Si, Ge or Sn) Compounds: Exchange Interaction Parameters of Ge and Sn. *Rev. Lat. Met. Mat.* **2017**, *37*, 27–34.
- (17) Nénert, G.; Palstra, T. T. M. Magnetolectric and Multiferroic Properties of Ternary Copper Chalcogenides $\text{Cu}_2\text{M}^{\text{II}}\text{M}^{\text{IV}}\text{S}_4$. *J. Phys.: Condens. Matter* **2009**, *21*, 176002.
- (18) Brant, J. A.; Clark, D. J.; Kim, Y. S.; Jang, J. I.; Zhang, J. H.; Aitken, J. A. $\text{Li}_2\text{CdGeS}_4$, A Diamond-Like Semiconductor with Strong Second-Order Optical Nonlinearity in the Infrared and Exceptional Laser Damage Threshold. *Chem. Mater.* **2014**, *26*, 3045–3048.
- (19) Jang, J. I.; Clark, D. J.; Brant, J. A.; Aitken, J. A.; Kim, Y. S. Highly efficient infrared optical nonlinearity of a wide-bandgap chalcogenide $\text{Li}_2\text{CdGeS}_4$. *Opt. Lett.* **2014**, *39*, 4579.
- (20) Bernert, T.; Pfitzner, A. $\text{Cu}_2\text{MnM}^{\text{IV}}\text{S}_4$ ($\text{M}^{\text{IV}} = \text{Si, Ge, Sn}$) - analysis of crystal structures and tetrahedra volumes of normal tetrahedral compounds. *Z. Kristallogr.* **2005**, *220*, 968–972.
- (21) Kirkham, M.; Heroux, L.; Ruiz-Rodriguez, M.; Huq, A. AGES: Automated Gas Environment System for *in Situ* Neutron Powder Diffraction. *Rev. Sci. Instrum.* **2018**, *89*, 092904.
- (22) Rodríguez-Carvajal, J. Recent Advances in Magnetic Structure Determination by Neutron Powder Diffraction. *Phys. B Condens. Matter* **1993**, *192*, 55–69.
- (23) Perez-Mato, J. M.; Gallego, S. V.; Tasci, E. S.; Elcoro, L.; de la Flor, G.; Aroyo, M. I. Symmetry-Based Computational Tools for Magnetic Crystallography. *Annu. Rev. Mater. Res.* **2015**, *45*, 217–248.
- (24) Sheldrick, G. M. A short history of SHELX. *Acta Crystallogr., Sect. A: Found. Crystallogr.* **2008**, *64*, 112–122.
- (25) McGowan, R. J. Attenuated Total Reflectance vs. Transmission Infrared Spectrometry in the Quantitative Evaluation of Paint Vehicles. *Anal. Chem.* **1963**, *35*, 1664–1665.
- (26) Zhang, J. H.; Clark, D. J.; Brant, J. A.; Rosmus, K. A.; Grima, P.; Lekse, J. W.; Jang, J. I.; Aitken, J. A. $\alpha\text{-Li}_2\text{ZnGeS}_4$: A Wide-Bandgap Diamond-like Semiconductor with Excellent Balance between Laser-Induced Damage Threshold and Second Harmonic Generation Response. *Chem. Mater.* **2020**, *32*, 8947–8955.
- (27) Blaha, P.; Schwarz, K.; Tran, F.; Laskowski, R.; Madsen, G. K. H.; Marks, L. D. WIEN2k: An APW+lo Program for Calculating the Properties of Solids. *J. Chem. Phys.* **2020**, *152*, 074101.
- (28) Perdew, J. P.; Burke, K.; Ernzerhof, M. Generalized Gradient Approximation Made Simple. *Phys. Rev. Lett.* **1996**, *77*, 3865–3868.
- (29) Anisimov, V. I.; Solov'ev, I. V.; Korotin, M. A.; Czyżyk, M. T.; Sawatzky, G. A. Density-Functional Theory and NiO Photoemission Spectra. *Phys. Rev. B* **1993**, *48*, 16929–16934.
- (30) Anisimov, V. I.; Aryasetiawan, F.; Lichtenstein, A. I. First-principles calculations of the electronic structure and spectra of strongly correlated systems: the LDA+U method. *J. Phys.: Condens. Matter* **1997**, *9*, 767–808.
- (31) Biniskos, N.; dos Santos, F. J.; Schmalzl, K.; Raymond, S.; dos Santos Dias, M.; Persson, J.; Marzari, N.; Blügel, S.; Lounis, S.; Brückel, T. Complex magnetic structure and spin waves of the noncollinear antiferromagnet Mn_3Si_2 . *Phys. Rev. B* **2022**, *105*, 104404.
- (32) Shannon, R. D. Revised Effective Ionic Radii and Systematic Studies of Interatomic Distances in Halides and Chalcogenides. *Acta Crystallogr.* **1976**, *32*, 751–767.
- (33) Guen, L.; Glaunsinger, W. S. Electrical, magnetic, and EPR studies of the quaternary chalcogenides $\text{Cu}_2\text{A}^{\text{II}}\text{B}^{\text{IV}}\text{X}_4$ prepared by iodine transport. *J. Solid State Chem.* **1980**, *35*, 10–21.
- (34) Gulay, L. D.; Nazarchuk, O. P.; Oleksyuk, I. D. Crystal structures of the compounds $\text{Cu}_2\text{CoSi}(\text{Ge,Sn})\text{S}_4$ and $\text{Cu}_2\text{CoGe}(\text{Sn})\text{-Se}_4$. *J. Alloys Compd.* **2004**, *377*, 306–311.
- (35) Chourio, M.; Romero, H.; Betancourt, L.; Sagredo, V. Crystal Growth and Magnetic Properties of the $\text{Cu}_2\text{MnGeS}_4$ Semiconductor. *New Trends Magn., Magn. Mater., Their Appl.* **1994**, *2*, 359–363.
- (36) Shapira, Y.; McNiff, E. J.; Oliveira, N. F.; Honig, E. D.; Dwight, K.; Wold, A. Magnetic properties of $\text{Cu}_2\text{Zn}_{1-x}\text{Mn}_x\text{GeS}_4$: Antiferromagnetic interactions in the wurtz-stannite structure. *Phys. Rev. B* **1988**, *37*, 411–418.
- (37) Delgado, G. E.; Sagredo, V. Synthesis and crystal structure of the quaternary semiconductor $\text{Cu}_2\text{NiGeS}_4$, a new stannite-type compound. *Rev. Mex. Fis.* **2019**, *65*, 355–359.
- (38) Beraich, M.; Shaili, H.; Benhsina, E.; Hafidi, Z.; Taibi, M.; Bentiss, F.; Guenbour, A.; Bellaouchou, A.; Mzerd, A.; Zarrouk, A.; Fahoume, M. Experimental and theoretical study of new kesterite $\text{Cu}_2\text{NiGeS}_4$ thin film synthesized via spray ultrasonic technic. *Appl. Surf. Sci.* **2020**, *527*, 146800.
- (39) Allemand, J.; Wintenberger, M. Propriétés structurales et magnétiques de quelques composés du type stannite. *Bull. Soc. Fr. Mineral. Cristallogr.* **1970**, *93*, 14–17.
- (40) Caneschi, A.; Cipriani, C.; Benedetto, F.; Sessoli, R. Characterisation of the antiferromagnetic transition of $\text{Cu}_2\text{FeSnS}_4$, the synthetic analogue of stannite. *Phys. Chem. Miner.* **2004**, *31*, 190–193.
- (41) Ganiel, U.; Hermon, E.; Shtrikman, S. Studies of magnetic ordering in $\text{Cu}_2\text{FeSnS}_4$ by Mössbauer spectroscopy. *J. Phys. Chem. Solids* **1972**, *33*, 1873–1878.
- (42) Bernardini, G. P.; Borriani, D.; Caneschi, A.; Di Benedetto, F.; Gatteschi, D.; Ristori, S.; Romanelli, M. EPR and SQUID magnetometry study of $\text{Cu}_2\text{FeSnS}_4$ (stannite) and $\text{Cu}_2\text{ZnSnS}_4$ (kesterite). *Phys. Chem. Miner.* **2000**, *27*, 453–461.
- (43) Rincón, C.; Quintero, M.; Moreno, E.; Power, Ch.; Quintero, E.; Henao, J. A.; Macías, M. A.; Delgado, G. E.; Tovar, R.; Morocoima, M. X.-R. X-ray diffraction, Raman spectrum and magnetic susceptibility of the magnetic semiconductor $\text{Cu}_2\text{FeSnS}_4$. *Solid State Commun.* **2011**, *151*, 947–951.
- (44) Brant, J. A.; dela Cruz, C.; Yao, J.; Douvalis, A. P.; Bakas, T.; Sorescu, M.; Aitken, J. A. Field-Induced Spin-Flop in Antiferromagnetic Semiconductors with Commensurate and Incommensurate Magnetic Structures: $\text{Li}_2\text{FeGeS}_4$ (LIGS) and $\text{Li}_2\text{FeSnS}_4$ (LITS). *Inorg. Chem.* **2014**, *53*, 12265–12274.
- (45) Kurtz, S. K.; Perry, T. T. A Powder Technique for the Evaluation of Nonlinear Optical Materials. *IEEE J. Quantum Electron.* **1968**, *39*, 3798–3813.
- (46) Ohmer, M. C.; Pandey, R. Emergence of Chalcopyrites as Nonlinear Optical Materials. *MRS Bull.* **1998**, *23*, 16–22.
- (47) Jackson, A. G.; Ohmer, M. C.; LeClair, S. R. Relationship of the Second Order Nonlinear Optical Coefficient to Energy Gap in Inorganic Non-Centrosymmetric Crystals. *Infrared Phys. Technol.* **1997**, *38*, 233–244.
- (48) Sinagra, C. W.; Saouma, W., III; Otieno, F. O.; Lapidus, C. O.; Zhang, S. H.; Craig, J.-H.; Grima-Gallardo, A. J.; Brant, P.; Rosmus, J. A.; Rosello, K. A.; Jang, K. E.; Aitken, J. I.; Aitken, J. A. Synthesis, structure, linear and nonlinear optical properties of noncentrosymmetric quaternary diamond-like semiconductors, $\text{Cu}_2\text{ZnGeS}_4$ (CZGSe) and the novel $\text{Cu}_4\text{ZnGe}_2\text{Se}_7$. *J. Alloys Compd.* **2021**, *888*, 161499.
- (49) Brant, J. A.; Clark, D. J.; Kim, Y. S.; Jang, J. I.; Weiland, A.; Aitken, J. A. Outstanding Laser Damage Threshold in $\text{Li}_2\text{MnGeS}_4$ and Tunable Optical Nonlinearity in Diamond-Like Semiconductors. *Inorg. Chem.* **2015**, *54*, 2809–2819.
- (50) Fukushima, T.; Yamauchi, K.; Picozzi, S. Magnetically Induced Ferroelectricity in $\text{Cu}_2\text{MnSnS}_4$ and $\text{Cu}_2\text{MnSnSe}_4$. *Phys. Rev. B: Condens. Matter Phys.* **2010**, *82*, 014102.
- (51) Zhu, L.; Li, L.; Cheng, T.-M. First principle study of the electrochemical properties of $\text{Li}_2\text{FeSiS}_4$. *Comput. Mater. Sci.* **2015**, *106*, 135–139.
- (52) Beraich, M.; Shaili, H.; Hafidi, Z.; Benhsina, E.; Majdoubi, H.; Taibi, M.; Guenbour, A.; Bellaouchou, A.; Mzerd, A.; Bentiss, F.; Zarrouk, A.; Fahoume, M. Facile synthesis of the wurtz stannite (orthorhombic) $\text{Cu}_2\text{MnGeS}_4$ thin film via spray ultrasonic method:

Structural, Raman, optical and electronic study. *J. Alloys Compd.* **2020**, *845*, 156216.

(53) El Hamdaoui, J.; El-Yadri, M.; Lakaal, K.; Kria, M.; Courel, M.; Ojeda, M.; Pérez, L. M.; Laroze, D.; Feddi, E. Ab initio study on electronic and optical properties of $\text{Cu}_2\text{NiGeS}_4$ for photovoltaic applications. *Sol. Energy* **2022**, *237*, 333–339.

(54) Chen, R.; Persson, C. Electronic and optical properties of Cu_2XSnS_4 ($X = \text{Be, Mg, Ca, Mn, Fe, and Ni}$) and the impact of native defect pairs. *J. Appl. Phys.* **2017**, *121*, 203104.

(55) Bourges, C.; Al Rahal Al Orabi, R.; Miyazaki, Y. Off-stoichiometry effect on thermoelectric properties of the new p-type sulfides compounds $\text{Cu}_2\text{CoGeS}_4$. *J. Alloys Compd.* **2020**, *826*, 154240.

(56) Zhang, D.; Yang, J.; Jiang, Q.; Zhou, Z.; Li, X.; Xin, J.; Basit, A.; Ren, Y.; He, X. Multi-cations compound $\text{Cu}_2\text{CoSnS}_4$: DFT calculating, band engineering and thermoelectric performance regulation. *Nano Energy* **2017**, *36*, 156–165.

(57) Azam, S.; Khan, S. A.; Goumri-Said, S. DFT study of optoelectronic and magnetic properties of iron-containing diamond-like materials $\text{Ag}_2\text{FeSiS}_4$, $\text{Li}_2\text{FeSnS}_4$, and $\text{Li}_2\text{FeGeS}_4$. *Solid State Sci.* **2017**, *72*, 71–79.

(58) Beraich, M.; Shaili, H.; Benhsina, E.; Hafidi, Z.; Mansouri, S.; Taibi, M.; Bentiss, F.; Guenbour, A.; Bellaouchou, A.; Mzerd, A.; Zarrouk, A.; Fahoume, M. Preparation and characterization of $\text{Cu}_2\text{FeGeS}_4$ thin-film synthesized via spray ultrasonic method – DFT study. *Mater. Lett.* **2020**, *275*, 128070.

(59) Rudisch, K.; Espinosa-García, W. F.; Osorio-Guillén, J. M.; Araujo, C. M.; Platzer-Björkman, C.; Scragg, J. J. S. Structural and Electronic Properties of $\text{Cu}_2\text{MnSnS}_4$ from Experiment and First-Principles Calculations. *Phys. Status Solidi B* **2019**, *256*, 1800743.

(60) Friedrich, D.; Greil, S.; Block, T.; Heletta, L.; Pöttgen, R.; Pfitzner, A. Synthesis and Characterization of $\text{Ag}_2\text{MnSnS}_4$, a New Diamond-like Semiconductor. *Z. Anorg. Allg. Chem.* **2018**, *644*, 1707–1714.

Recommended by ACS

Polar Bismuth Selenite Iodate Oxide BiSeIO_6 with Three Types of Lone Pair Cations in One Structure

Lei Geng, Changyu Meng, *et al.*

JANUARY 27, 2023
INORGANIC CHEMISTRY

READ 

Electrochemical Flux Synthesis of Type-I Na_8Si_6 Clathrates: Particle Size Control Using a Solid or Molten Na–Sn Mass Transport Mediator

Andrew Dopilka, Candace K. Chan, *et al.*

DECEMBER 22, 2022
INORGANIC CHEMISTRY

READ 

Graphene Oxide-Intercalated Microbial Montmorillonite to Moderate the Dependence of Nafion-Based PEMFCs in High-Humidity Environments

Ziyi Meng, Qingting Liu, *et al.*

JANUARY 24, 2023
ACS APPLIED ENERGY MATERIALS

READ 

Two Carboxylate-Cyanurates with Strong Optical Anisotropy and Large Band Gaps

Yan Chen, Jianggao Mao, *et al.*

JANUARY 23, 2023
INORGANIC CHEMISTRY

READ 

Get More Suggestions >